

# Zinc oxide incorporating iron nanoparticles with improved conductance and capacitance properties

N. Bouazizi<sup>1,2</sup> · F. Ajala<sup>3</sup> · M. Khelil<sup>4</sup> · H. Lachheb<sup>3</sup> · K. Khirouni<sup>4</sup> · A. Houas<sup>3,5</sup> · A. Azzouz<sup>2</sup>

Received: 8 May 2016 / Accepted: 20 June 2016 / Published online: 1 July 2016  
© Springer Science+Business Media New York 2016

**Abstract** Iron nanoparticles were incorporated into zinc oxide powders by an in situ dispersion method. The products were fully characterized by X-ray diffractometry, diffuse reflectance, FTIR spectrophotometry and complex impedance spectroscopy. The XRD patterns agreed with that of the ZnO typical wurtzite structure, the sharp diffraction peaks indicating good crystallinity of ZnO and ZnO-Fe nanoparticles. The average particle size determined by the Scherrer equation showed an increase from 20 to 25 nm for ZnO and ZnO-Fe respectively. The UV peak positions of the modified samples shifted to a longer wavelength compared to pure ZnO, providing evidence of changes in the acceptor level induced by iron nanoparticles. The optical band gap of the samples was found to be 3.14 eV for ZnO and 3.04 eV for ZnO-Fe. The electrical properties were investigated between 273 and 413 K, at several frequencies. Besides, a detailed analysis of the impedance spectrum showed an appreciable

improvement of the conductivity due to the addition of iron nanoparticles. The incorporation of Fe-NPs appears to be responsible for conductance variations, charge transfer and capacitance improvement. The above properties make these materials to be regarded as very promising electrode materials for high-efficiency energy storage.

## 1 Introduction

Semiconductor metal oxides have drawn much attention during the last decades due to their important features for many optoelectronic and gas sensor applications [1]. In such devices, semiconducting materials are supposed to act as charge transfer medium. The light-sensitive and charge transfer areas are usually separated. Transparent conducting zinc oxide (ZnO), which is a wide band gap semiconductor [2] has attracted growing interest due to the improvement in mechanical, thermal and gas barrier properties [3–6]. In fact, ZnO is attracted intensive importance not only because of its electrical and optical properties but also because of its various morphologies and energy conversion efficiency of solar cells based on ZnO [7, 8].

Efforts were devoted to improve the properties of ZnO nanoparticles by chemical modification of the molecular structure [9, 10]. In this regard, the size and morphology of ZnO are important parameters in determining the physical and chemical properties [11]. ZnO is a semi-conductor with a large gap band of 3.3 eV, and appears as an interesting alternative as a wide band gap material that can be easily synthesized in various nano-structured forms [12–15]. Hence, as a typical photoanode material, ZnO is environmentally friendly and has strong photogenerated hole oxidation ability, resulting in improved electron transfer efficiency and reduction of electron–hole recombination [16].

✉ N. Bouazizi  
bouazizi.nabil@hotmail.fr

✉ A. Azzouz  
azzouz.a@uqam.ca

<sup>1</sup> Research Unit: Environment, Catalyzes and Process Analysis, ENIG University of Gabes, Gabès, Tunisia

<sup>2</sup> Nanoqam, Department of Chemistry, University of Quebec at Montreal, Montreal, QC H3C 3P8, Canada

<sup>3</sup> Research Unit: Catalyzes and Materials for Environnement and Process, Faculty of Sciences, University of Gabes, Gabès, Tunisia

<sup>4</sup> Laboratory of Materials Physics and Nanomaterials Applied at Environment (LaPhyMNE), FSG University of Gabes, Gabès, Tunisia

<sup>5</sup> Department of Chemistry, IMSI University, Riyadh, Saudi Arabia

A variety of preparation routes have been devoted for the synthesis of metal oxide nanoparticles, such as magnetron sputtering, metal-organic chemical vapor deposition, pulsed-laser deposition, hydrothermal, molecular beam epitaxy and sol–gel process [17–19]. Among these methods, the sol–gel method has some advantages to prepare large area ZnO nanoparticles at low cost and easy technology [20, 21].

Compared to other methods, the sol–gel process is one of the most promising wet chemistry synthesis approaches. This method provides a favorable microenvironment for controlling the chemical reaction and it is possible to obtain a narrow nanoparticles size distribution, isotropic, and thermodynamically stable. In this study, ZnO nanoparticles were synthesized and modified by loading iron nanoparticles (Fe-NPs) into the lattice using an in situ dispersion method. The structural, optical and electrical properties of the resulting product ZnO-Fe were investigated by a combination of X-ray diffraction (XRD), diffuse reflectance spectroscopy (DRS), FT-IR spectrophotometry and complex impedance spectroscopy (CIS). Detailed studies on the electric, charge transfer and conduction mechanism were discussed at several temperatures and frequencies.

## 2 Experimental

### 2.1 Material synthesis

The synthesis of zinc oxide nanostructures was carried out using zinc acetate dehydrate and sodium acetate hydroxide as precursors. An aqueous solution of zinc acetate (0.2 M) was prepared, the colloidal solution was left stirring for 2 h, and then white precipitate was separated by centrifugation at room temperature. Several extractions, washings with water and ethanol were performed after every centrifugation to remove sodium acetate. The resulting powder was dried at 80 °C overnight and calcined at 600 °C. Fe<sup>0</sup>-NPs dispersion in ZnO powders was achieved using (Fe(NO<sub>3</sub>)<sub>3</sub> · 9H<sub>2</sub>O) as precursor in toluene (99.5 %,  $d = 0.865 \text{ g mL}^{-1}$ ) in the presence of hydrazine as the reducing agent. The resulting mixture turned black, indicating the formation of iron nanoparticles within ZnO. The latter product ZnO-Fe was dried at 35 °C for 6 h and then stored in sealed enclosure containing dry and oxygen-free nitrogen (Scheme 1).

### 2.2 Material characterization

ZnO and ZnO-Fe were fully characterized through powder X-ray diffraction (XRD) (Siemens D5000 X-ray

diffractometer and a Cu-K $\alpha$  radiation at  $\lambda = 1.54056 \text{ \AA}$ ) in the  $2\theta$  ranges of 30°–80°, Fourier transform IR were recorded using a KBr cell Fourier transformed IR equipment and infrared spectroscopy (NICOLET IR200), of wave ranged from 4000 to 400  $\text{cm}^{-1}$ . The band gap was assessed using UV–vis diffuse-reflectance spectrophotometry (DRS) recorded on a Sinco S-4100 spectrometer. Electrical measurements were performed using a two electrode configuration. The sample was compacted into pellets of 8 mm diameter and 1 mm thickness using 3 tons/ $\text{cm}^2$  uniaxial press. Electrical impedances were assessed in the frequency range [40 Hz–100 kHz] with a TEGAM 3550 ALF automatic bridge at room temperature. The variation of both real ( $Z'$ ) and imaginary ( $Z''$ ) parts of the complex impedance ( $Z^* = Z' - i Z''$ ) was investigated herein.

## 3 Results and discussions

### 3.1 Swelling properties of ZnO

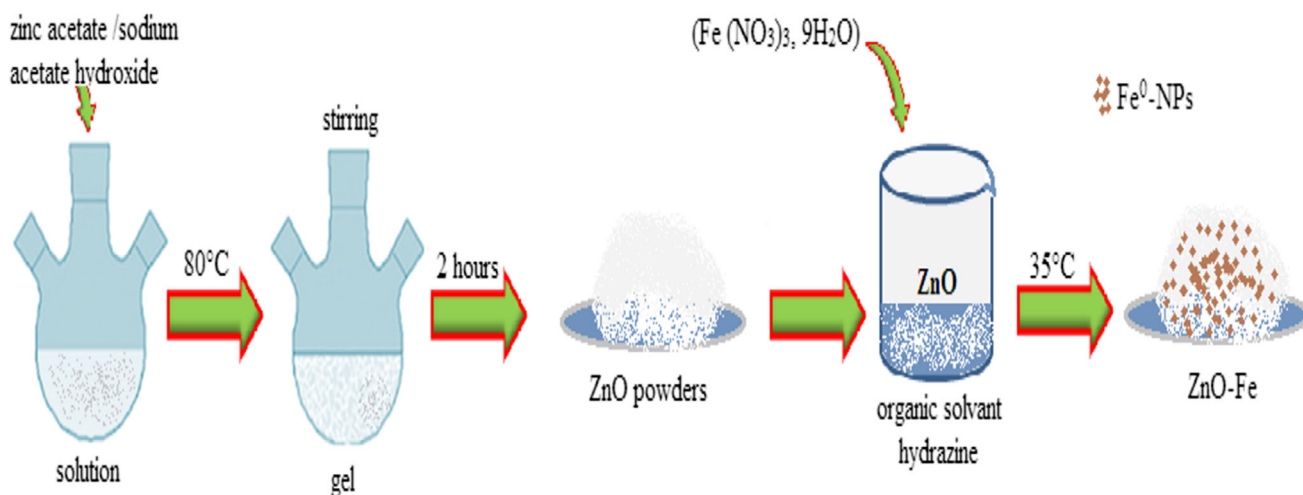
Figure 1 shows typical X-ray diffraction patterns of ZnO and ZnO-Fe, which were identified through their main reflexion peaks appearing at  $2\theta = 31.75^\circ, 34.60^\circ, 36.28^\circ, 47.30^\circ, 56.50^\circ, 61.96^\circ, 66.45^\circ, 67.90^\circ$  and  $69.80^\circ$ . These reflexions were assigned to (100), (002), (101), (102), (110), (103), (200), (112) and (201) plane families, respectively, and are in agreement with those of a typical würtzite structure ZnO (hexagonal phase, space group P6<sub>3</sub>mc, and JCPDS no. 36-1451) [22]. No other phase and no diffraction peaks from any other impurities were detected due to the low iron content of 0.3 wt%. The slight shifts of all line towards lower angles suggest that iron atoms are localized in the ZnO lattice.

The average grain size of zinc oxide was calculated by the Scherrer formula (1):

$$(D = 0.89\lambda/\beta\cos\theta) \quad (1)$$

where D is the crystallite size,  $\lambda$  is the wavelength (1.5406 Å for Cu K $\alpha$ ),  $\beta$  is the full-width at half-maximum of main intensity peak after subtraction of the equipment broadening and  $\theta$  is the diffraction angle. The mean grain size was found to be increased from 20 nm for ZnO to 25 nm for ZnO-Fe.

On the other hand, the lattice parameters was calculated and the unit cell parameters 'a' and 'c' obtained from the XRD data for all the samples are summarized in Table 1. As a result, for ZnO-Fe the lattice parameters 'a' and 'c' were found to undergo small changes, presumably due to slight distortion of ZnO lattice. These results can be explained by the electrostatic interactions between terminal



**Scheme 1** Synthesis method of the ZnO-Fe nanoparticles

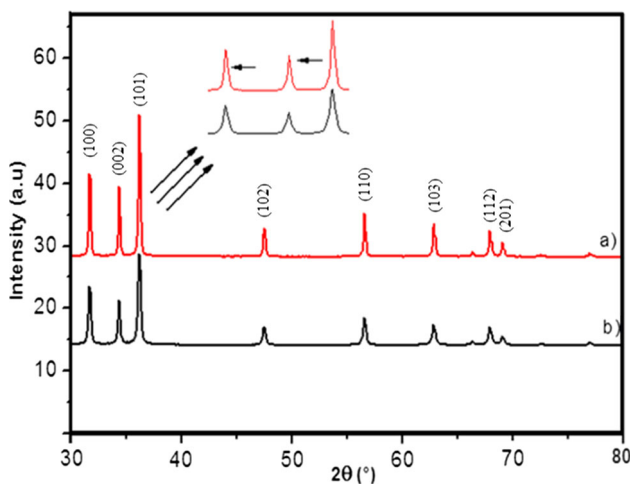


**Fig. 1** Powder X-ray diffraction patterns of ZnO *a*) and ZnO-Fe *b*)

**Table 1** Lattice parameters and crystallite size of pure and modified ZnO

Samples	Crystallite size (nm)	Lattice parameter	
		a(Å)	c(Å)
ZnO	20	3.139	4.979
ZnO-Fe	25	3.148	4.985

hydroxyl groups in the center of ZnO caused by the incorporation of iron nanoparticles.

### 3.2 FT-IR analysis

Figure 2 depicted the typical FT-IR spectrum of pure and modified ZnO. The characteristic peaks showed few well-defined bands appearing at 530, 1629 and 3426  $\text{cm}^{-1}$ . The broad absorption peaks between 3420 and 1640  $\text{cm}^{-1}$  were

associated to free OH stretching vibration. The occurrence of a band at 525  $\text{cm}^{-1}$  is due to stretching vibration of metal–oxygen bond. Indeed, another sharp peak around 1375  $\text{cm}^{-1}$  was associated to H–O–H bending vibration due to the presence of moisture in the samples [23]. The other two short peaks observed between 2330 and 2420  $\text{cm}^{-1}$  appear to be caused by the existence of  $\text{CO}_2$  molecule in air. The presence of iron nanoparticles can be tested by the lower peaks registered in the region varied between 1040 and 970  $\text{cm}^{-1}$ .

On the other hand, slight shifts towards higher wavenumbers of all bands were registered for ZnO-Fe. This provides evidence of an additional contribution of the Zn–OH stabilization effect. Here, these shifts are attributed to the interaction occurring between the lattice oxygen atoms with the iron nanoparticles.

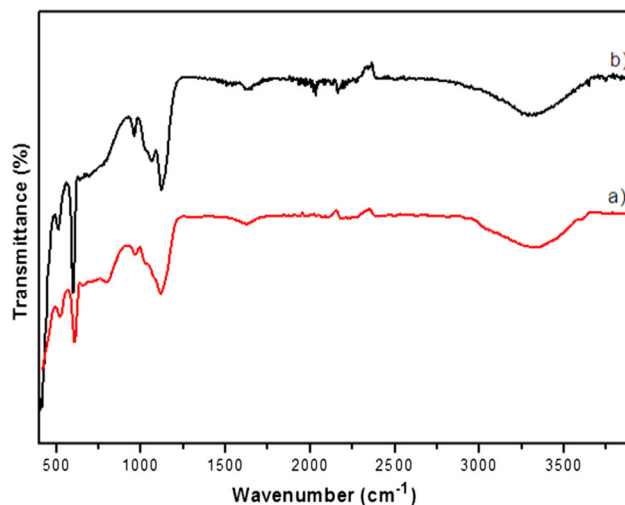


**Fig. 2** FTIR spectra of ZnO *a*) and ZnO-Fe *b*)

### 3.3 Optical properties

In order to study the optical switching behavior of ZnO and ZnO-Fe, the transmission spectra were measured in the range of 300–800 nm. Fig. 3 shows lower transmittance for ZnO-Fe as compared to ZnO in the wavelength range 400–800 nm. This decrease in the transmittance value accounts for shifts in the band gap towards lower energy after ZnO modification, and can be explained in terms of increase in the electron density around Fe-NPs.

The optical band-gap ( $E_g$ ) for these materials was determined from the sharply increasing absorption region according to Tauc and Menth’s method [24].

The plot  $(\alpha h\nu)^2$  versus  $h\nu$ , where  $\alpha$  is the constant related to the material,  $h$  - the Plank’s constant, and  $\nu$  - the photon frequency (Fig. 4). The experimentally estimated band gaps value was found to decrease from 3.14 eV (ZnO) to 3.04 eV after iron nanoparticles dispersion. This provides clear evidence of the transparent properties of ZnO-Fe, which suggests an improvement of the electrical properties and semiconductor character.

### 3.4 Impedance analysis

The complex impedance spectra ( $Z''$  vs  $Z'$ ) of ZnO and ZnO-Fe for several temperatures are shown in Figs. 5 and 6. From Fig. 5 a single semicircular response was noticed, indicating that no grain boundaries or electrode effects are involved in the patterns. The fact that the semicircular centers are below the real axis indicates a non-Debye type of relaxation [25].

However, Fe-NPs incorporation was found to induce strong improvement of the electrical properties of ZnO, as supported by the visible curve arrangement in a semicircle

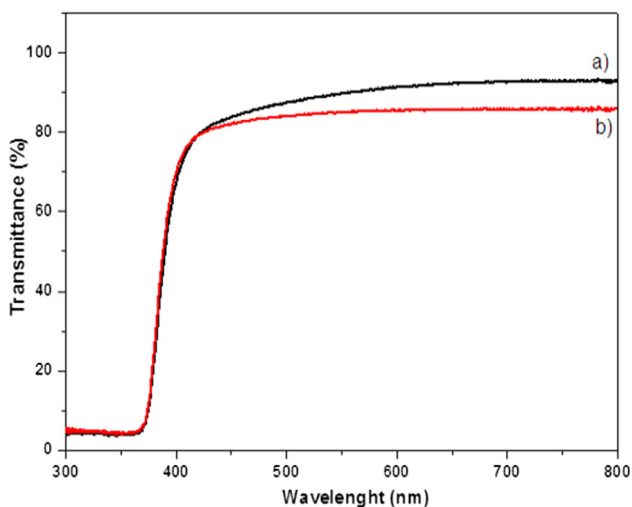


Fig. 3 Transmission spectra of ZnO a) and ZnO-Fe b)

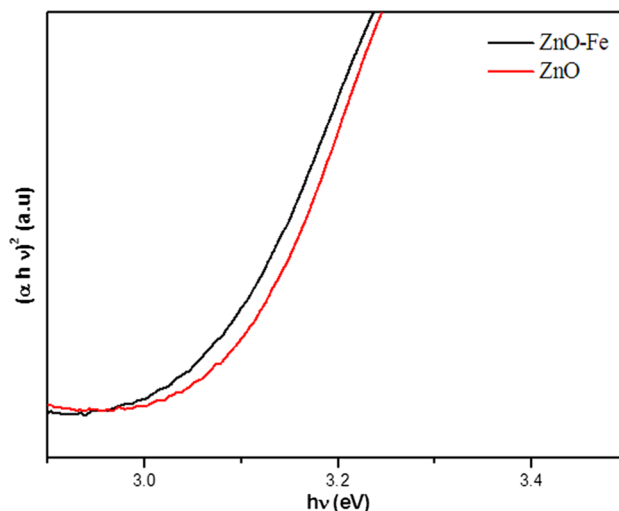


Fig. 4 Plot of  $(\alpha h\nu)^2$  versus  $h\nu$  of ZnO and ZnO-Fe

at low  $Z'$  values. This can be attributed to the film impedance observed at low frequency, associated to a polarization phenomenon. As a result, the radii of the semicircles decreased with increasing temperature. Here, these radius changes are a precise indicator of the thermal activation of the conduction mechanism. Additionally, at high frequency range, the newly appeared line corresponds to a Warburg impedance, which is due to electron diffusion at the pellet-electrodes [26].

### 3.5 Relaxation proprieties

Figure 7 shows the variation of the real ( $Z'$ ) and imaginary ( $Z''$ ) parts of impedance of pure ZnO. At low frequencies, both amplitudes of  $Z'$  and  $Z''$  were found to decrease with the rise in temperature and then all curves merge at high-

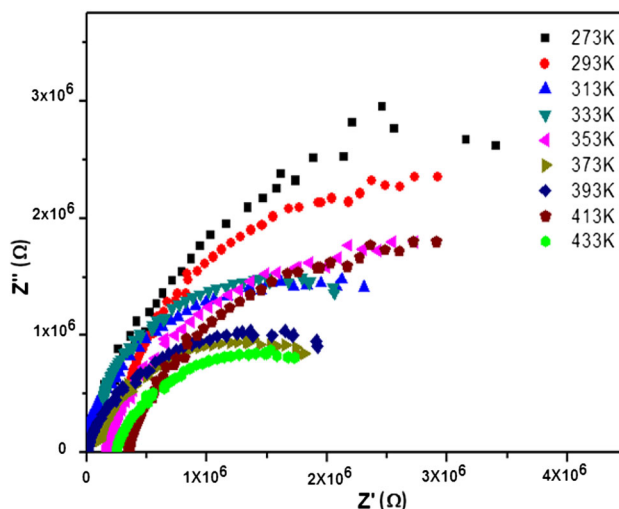
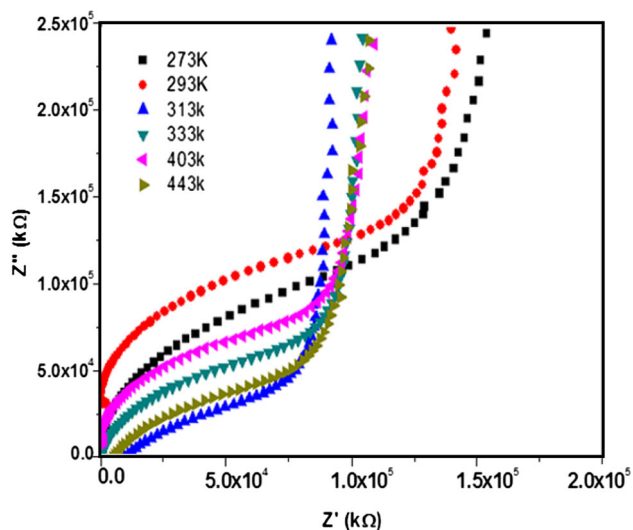


Fig. 5 Cole-Cole plots of ZnO at various temperatures



**Fig. 6** Cole-Cole plots of ZnO-Fe at various temperatures

frequency region. This decrease can be explained by an increased conductivity and the possible release of space charges.

However, with decreasing frequencies,  $Z''$  increased to reach a peak ( $Z''$  max) and then decreased as the frequencies rise at different temperatures. Consequently, this behavior lowers the barrier properties in the materials and such a thorough modification of the ZnO surface properties is often explained in terms of activated electron charge due to the increase of temperature [27].

On the other hand, the changes of  $Z'$  and  $Z''$  parts of impedance registered for ZnO-Fe show a decrease in  $Z'$  at various temperatures (Fig. 8). Here, high  $Z'$  values were noticed at low frequencies, presumably due to an accumulation of free charges at the pellet-electrode interface. Afterwards, all the curves were merged in high-frequency region and  $Z'$  becomes independent of frequencies. Moreover, the variation of  $Z''$  with frequency revealed  $Z''$  maximum values ( $Z''$  max), which shifted to higher frequencies with increasing temperature. The broadening of these shifts towards higher frequency indicates the presence of electrical relaxation phenomenon, which appears to decrease with increasing temperature [25]. This result allows stating that most Fe-NPs are inserted within the ZnO lattice, and their present on the external surface should play only a minor role in the improvement of the conduction phenomenon. In addition, Fe-NPs and Zn-O deprotonation seems to be responsible of this effect. However, in highly crystalline ZnO, protons are mainly located at the structure edges, and this is why one strongly believes that metal-lattice oxygen interactions should also be taken into account. After this frequency threshold, both

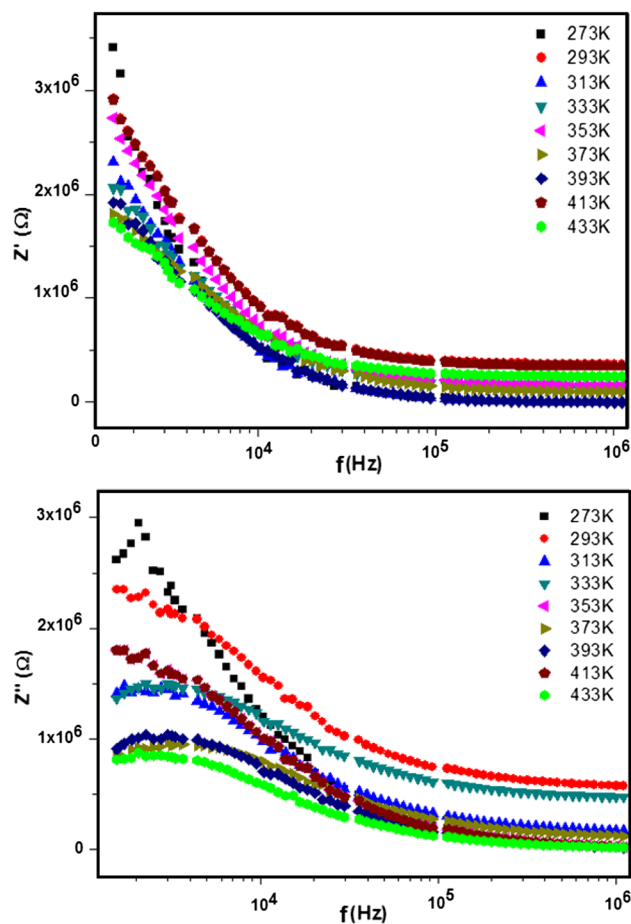


**Fig. 7** Angular frequency dependence of  $Z'$  and  $Z''$  for ZnO

curves merged, and tend towards zero at higher frequency. In summary, the higher semicircle radius observed for ZnO-Fe as compared to that of its pure counterpart suggests an increased electron transfer resistance after Fe-NPs incorporation.

### 3.6 Conductance change

ZnO is a well-known n-type semiconductor and the dependence of conductivity on frequency and temperature are very important to understand the electron transport mechanism. The variation of conductance vs temperatures of ZnO and ZnO-Fe at several frequencies is shown in Figs. 9 and 10. At low temperatures, the conductance was constant and started growing when  $T > 293$  K. For each temperature, the crossover frequency was characterized by a slope change at certain frequency values, known as hopping frequencies [28]. Herein, the content of iron nanoparticles was found to induce an increase in conductance with increasing temperature. This corresponds to a semiconductor behavior.

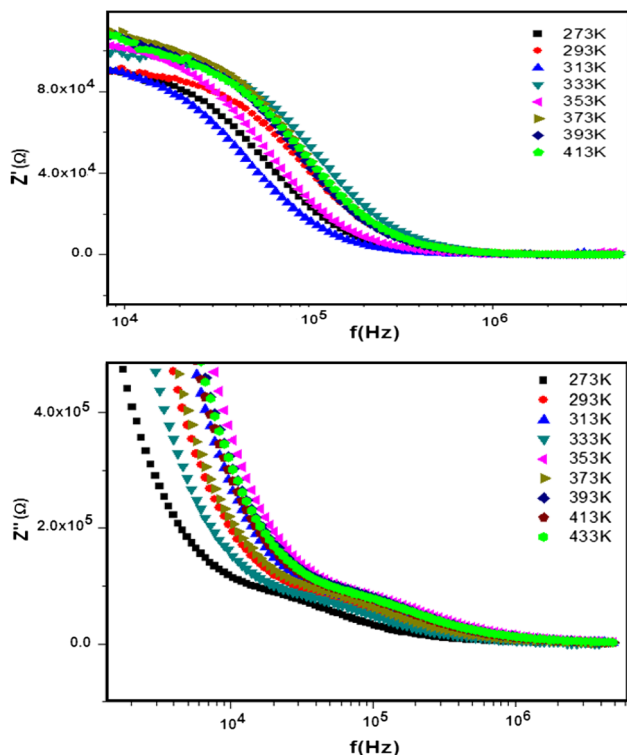


Fig. 8 Angular frequency dependence of  $Z'$  and  $Z''$  for ZnO-Fe

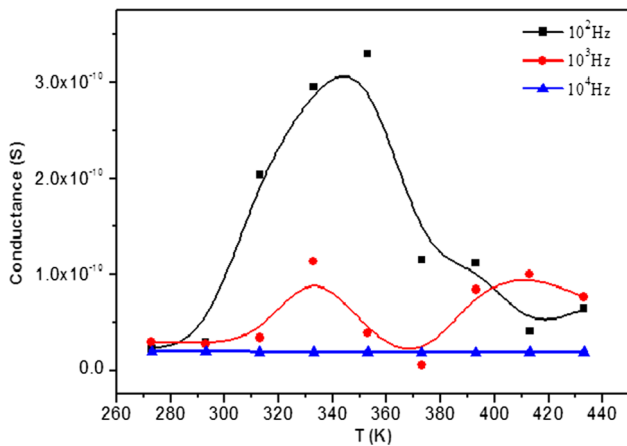


Fig. 9 Conductance as a function of temperatures for ZnO

In addition, this common behavior of different classes of materials was already pointed out by Jonscher, who referred to it as universal dynamic response [29]:

$$G(\omega) = G_{dc} + A\omega^s \tag{2}$$

where,  $G_{dc}$  is the conductivity at low frequencies,  $A$  - a constant,  $\omega = 2\pi f$  and  $s$  is an exposing which frequency dependent. The resulting measurements of conductance at several frequencies reveal that the conductance achieved  $1.75 \times 10^{-7}$  S for ZnO-Fe contrariwise  $3 \times 10^{-10}$  S recorded for pure ZnO. By referring to these values, it can

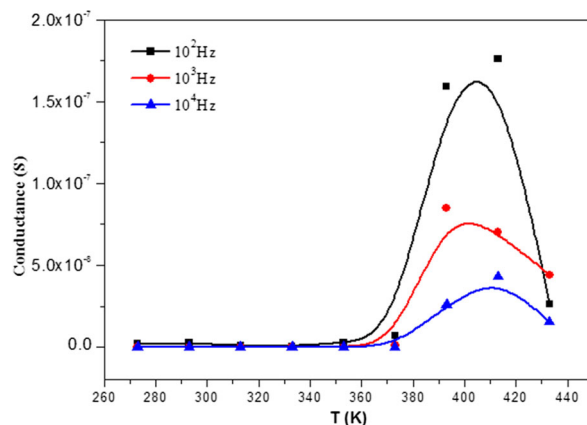


Fig. 10 Conductance as a function of temperature for ZnO-Fe

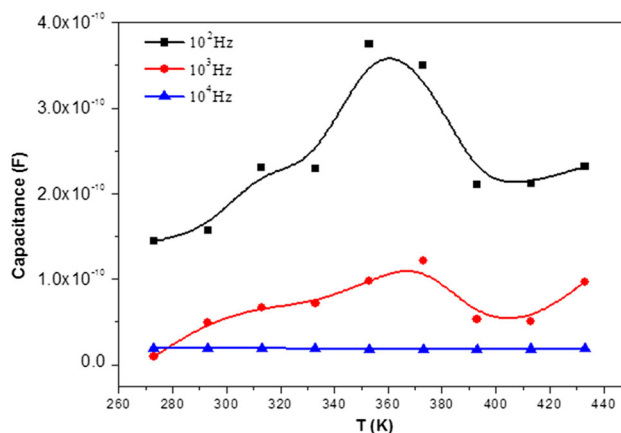
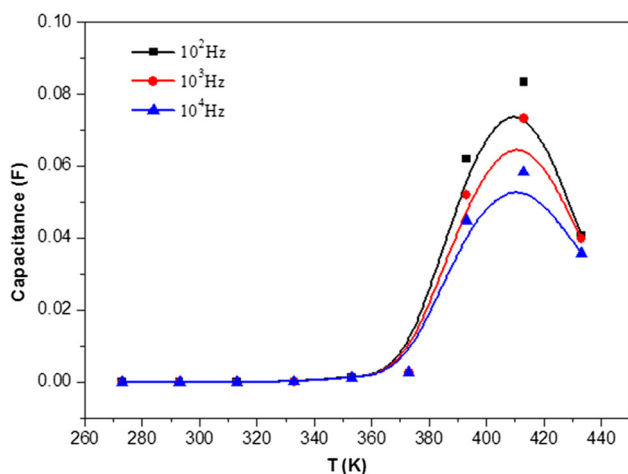


Fig. 11 Capacitance versus temperature for ZnO

be concluded that proton conduction is involved in such materials, according to the Grotthuss mechanism. All these facts contribute to the visible improvement of the conductivity by the appreciable dispersion of Fe-NPs [30]. The maximum value of ZnO-Fe conductance was obtained at about  $10^{-4}$  S loading content, which indicates the existence of an active effect induced by Fe-NPs. However, the minimum of the conductance value ( $10^{-6}$  S) was explained by the blocking effect on the charge carrier transport process resulting from ZnO-Fe particle aggregation. This phenomenon is expected to reduce the conductivity of the constant phase elements.

The above results allow concluding that the observed shifts arise from a thermally activated process. Furthermore, the conductivity dependence on frequency indicates the hopping conduction at higher frequencies between localized states. Additionally, the high-frequency dependence of the conductivity was often observed experimentally in most polar semiconductor oxides, This must be to the assumption of thermally activated hopping of charge



**Fig. 12** Capacitance versus temperature for ZnO-Fe

carriers between localized sites over the potential barrier that correlates its sites [31].

### 3.7 Capacitance measurements

In order to investigate the role of Fe-NPs incorporation on the charge transfer phenomenon, the capacitance measurements at several frequencies were plotted in Figs. 11 and 12). The capacitance of ZnO and ZnO-Fe decreased with increasing frequency. The capacitance accumulation decreased with fluctuation for ZnO. The capacitance of ZnO-Fe was found to be almost proportional to the frequency up to a maximum level. The high capacitance at low frequencies can be explained by the charge ability to follow the applied signal. However, the decrease in capacitance at higher frequencies indicates that the charge at the interface may not follow conductivity signal [32].

Consequently, it appears that the insertion of iron nanoparticles enhances the charge transfer due to their high electron density. Besides, the surface functional groups also improved the electrical double layer capacitance formed by charge separation on the interface between the pellet and the electrode. Here, the effect of the amount of functional groups on the capacitance still remains to be elucidated.

However, research is still in progress in this regard, assuming that the negative electron charge is balanced by positive (hole) charges accumulated near the surface. Increasing frequency ought to induce hole depletion. Here, the capacitance change is expected to directly correlate with the amount of dispersed Fe-NPs within the lattice of ZnO. The results obtained herein allow concluding that shifts towards higher frequency account for a depletion in charge holes on the surface. Therefore, the capacitance decay recorded for ZnO-Fe in the high frequencies region

indicates a charge carrier capacity of the pellet interface at moderate frequency that follows the conductivity.

## 4 Conclusions

The present study demonstrated the Fe-NPs insertion effect on the structural, optical and electrical properties of ZnO lattice. Crystallite size and lattice parameters changes were observed in the presence of Fe-NPs. UV–visible diffuse reflectance revealed a shift of the band-gap energy, as a first precise indicator of the genesis of electrical property. It was clearly demonstrated that incorporation of small amount of iron nanoparticles confers electrical properties to ZnO. Besides,  $Z'$  and  $Z''$  measurements revealed a semiconductor behavior and an occurrence of a relaxation phenomenon at several temperatures. The Fe-loaded ZnO material displayed conductivity due to the formation of effective proton-conducting and the proton transfer between Fe-NPs within the lattice. Additionally, it was concluded that Fe-NPs contribute to the capacitance of ZnO electrode, which enhances electron double layer capacitance.

## References

1. K.H. Kim, Z. Jin, Y. Abe, M. Kawamura, Effect of Li and Cu dopants on structural properties of zinc oxide nanorods. *Superlattice Microstruct.* **77**, 101–107 (2015)
2. C.E. Benouis, M. Benhaliliba, A. Sanchez Juarez, M.S. Aida, F. Chami, F. Yakuphanoglu, The effect of indium doping on structural, electrical conductivity, photoconductivity and density of states properties of ZnO films. *J. Alloys Compd.* **490**, 62–67 (2010)
3. K.H. Kim, T. Umakoshi, Y. Abe, M. Kawamura, T. Kiba, Growth behavior of Al-doped zinc oxide microrods with times. *Superlattices Microstruct.* **85**, 743–746 (2015)
4. K.H. Kim, T. Umakoshi, Y. Abe, M. Kawamura, T. Kiba, Determination of effective growth time for zinc oxide nanorods using chemical solution deposition. *Superlattices Microstruct.* **88**, 150–153 (2015)
5. B.C. Yadav, R. Srivastava, C.D. Dwivedi, P. Pramanik, Moisture sensor based on ZnO nanomaterial synthesized through oxalate route. *Sens. Actuators B: Chemical* **131**, 216–222 (2008)
6. C. Shang, A. Barnabe, Structural study and phase transition investigation in a simple synthesis of porous architected-ZnO nanopowder. *Mater. Charact.* **86**, 206–211 (2013)
7. S. Erten-Ela, S. Cogal, S. Icli, Conventional and microwave-assisted synthesis of ZnO nanorods and effects of PEG<sub>400</sub> as a surfactant on the morphology. *Inorg. Chim. Acta* **362**, 1855–1858 (2009)
8. Z.L. Wang, Zinc oxide nanostructures: growth, properties and applications. *J. Phys.: Condens. Matter* **16**, 829–858 (2004)
9. S. Xu, Z.L. Wang, One-dimensional ZnO nanostructures: solution growth and functional properties. *Nano Res.* **4**(11), 1013–1098 (2011)

10. D.L. Raimondi, E. Kay, High resistivity transparent ZnO thin films. *J. Vac. Sci. Technol.* **1**, 96–99 (1970)
11. Z. Hu, G. Oskam, P.C. Searson, Influence of solvent on the growth of ZnO nanoparticles. *J. Colloid Interface Sci.* **263**, 454 (2003)
12. B. Liu, H.C. Zeng, Room temperature solution synthesis of monodispersed single-crystalline ZnO nanorods and derived hierarchical nanostructures. *Langmuir* **20**, 4196 (2004)
13. N. Bouazizi, F. Ajala, A. Bettaibi, M. Khelil, A. Benghnia, R. Bargougui, S. Louhichi, L. Labiadh, R.B. Slama, B. Chaouachi, K. Khirouni, A. Houas, A. Azzouz, Metal-organo-zinc oxide materials: investigation on the structural, optical and electrical properties. *J. Alloys Compd.* **25**, 146–153 (2016)
14. M.N. Romyantseva, E.A. Makeeva, A.M. Gaskov, Influence of the microstructure of semiconductor sensor materials on oxygen chemisorption on their surface. *Russ. J. Gen. Chem.* **78**, 2556–2565 (2008)
15. Y. Bu, Z. Chen, W. Li, B. Hou, Highly efficient photocatalytic performance of graphene-ZnO quasi-shell-core composite material. *ACS Appl. Mater. Interfaces* **5**, 12361 (2013)
16. L.H. Van, M.H. Hong, J. Ding, Structural and magnetic property of Co-doped-ZnO thin films prepared by pulsed laser deposition. *J. Alloys Compd.* **449**, 207 (2008)
17. N. Bouazizi, R. Bargougui, T. Boudharaa, M. Khelil, A. Benghnia, L. Labiadh, R.B. Slama, B. Chaouachi, S. Ammar, A. Azzouz, Synthesis and characterization of SnO<sub>2</sub> HMD-Fe materials with improved electric properties and affinity towards hydrogen. *Ceram. Int.* **42**, 9413–9418 (2016)
18. R. Bargougui, N. Bouazizi, W.B. Soltan, A. Gadri, A. Azzouz, S. Ammar, Controlled synthesis and electrical conduction properties of anatase TiO<sub>2</sub> nanoparticles via the polyol method. *Appl. Phys. A* **122**, 1–10 (2016)
19. K.J. Chen, F.Y. Hung, S.J. Chang, S.J. Young, Optoelectronic characteristics of UV photodetector based on ZnO nanowire thin films. *J. Alloys Compd.* **479**, 674 (2009)
20. F. Yakuphanoglu, Electrical and photovoltaic properties of cobalt doped zinc oxide nanofiber/n-silicon diode. *J. Alloys Compd.* **494**, 451 (2010)
21. R. Lamba, A. Umar, S.K. Mehta, S.K. Kansal, CeO<sub>2</sub> ZnO hexagonal nanodisks: efficient material for the degradation of direct blue 15 dye and its simulated dye bath effluent under solar light. *J. Alloys Compds.* **620**, 67–73 (2015)
22. J. Tauc, A. Menth, States in the gap. *J. Non-Cryst. Solids* **8**, 569 (1972)
23. S.A. Khayyat, M.S. Akhtar, A. Umar, ZnO nanocapsules for photocatalytic degradation of thionine, ZnO nanocapsules for photocatalytic degradation of thionine. *Mater. Lett.* **81**, 239–241 (2012)
24. M. Ram, Synthesis and electrical properties of (LiCo<sub>3/5</sub> Fe<sub>1/5</sub> Mn<sub>1/5</sub>) VO<sub>4</sub> ceramics. *Solid State Sci.* **12**, 350–354 (2010)
25. N. Bouazizi, R. Bargougui, A. Oueslati, R. Benslama, Effect of synthesis time on structural, optical and electrical properties of CuO nanoparticles synthesized by reflux condensation method. *Adv. Mater. Lett.* **6**, 158–164 (2015)
26. N. Bouazizi, R. Ouargli, S. Nousir, R. Benslama, A. Azzouz, Properties of SBA-15 modified by iron nanoparticles as potential hydrogen adsorbents and sensors. *J. Phys. Chem. Solid* **77**, 172–177 (2015)
27. B.N. Parida, P.R. Das, R. Padhee, R.N.P. Choudhary, Ferroelectric and pyroelectric properties of rare earth based tungsten-bronze compounds. *J. Mater. Sci.: Mater. Electron.* **3**, 0744 (2012)
28. R. Bargougui, A. Oueslati, G. Schmerber, C. Ulhaq-Bouillet, S. Colis, F. Hlel, S. Ammar, A. Dinia, Structural, optical and electrical properties of Zn-doped SnO<sub>2</sub> nanoparticles synthesized by the co-precipitation technique. *J. Mater. Sci.: Mater. Electron.* **25**, 2066–2071 (2014)
29. W.A. England, M.G. Cross, A. Hamnett, P.J. Wiseman, J.B. Goodenough, Fast proton conduction in inorganic ion-exchange compounds. *J. Solid State Ion.* **1**, 231 (1980)
30. T. Nagata, T. Shimura, A. Ashida, N. Fujimura, T. Ito, Electro-optic property of ZnO: X (X = Li, Mg) thin films. *J. Cryst. Growth* **237–239**, 533–537 (2002)
31. C.K. Maiti, S.K. Samanta, G.K. Dalapati, S.K. Nandi, S. Chatterjee, Electrical characterization of TiO<sub>2</sub> gate oxides on strained-Si. *J. Microelectron. Eng.* **72**, 253 (2004)
32. K.K. Saini, S.D. Sharma, C. Kanth, M. Kar, D. Singh, C.P. Sharma, Structural and optical properties of TiO<sub>2</sub> thin films derived by sol-gel dip coating process. *J. Non-Cryst. Solids* **353**, 2469 (2007)